Magnetization dynamics and spin pumping induced by standing elastic waves

A. V. Azovtsev and N. A. Pertsev
Ioffe Institute, 194021 St. Petersburg, Russia

(Received 17 December 2015; revised manuscript received 31 March 2016; published 1 November 2016)

The magnetization dynamics induced by standing elastic waves excited in a thin ferromagnetic film is described with the aid of micromagnetic simulations taking into account the magnetoelastic coupling between spins and lattice strains. Our calculations are based on the numerical solution of the Landau-Lifshitz-Gilbert equation comprising the damping term and the effective magnetic field with all relevant contributions. The simulations have been performed for 2-nm-thick $Fe_{81}Ga_{19}$ film dynamically strained by longitudinal and transverse standing waves with various frequencies, which span a wide range around the resonance frequency ν_{res} of coherent magnetization precession in unstrained $Fe_{81}Ga_{19}$ film. It is found that standing elastic waves give rise to complex local magnetization dynamics and spatially inhomogeneous dynamic patterns in the form of *standing spin waves* with the same wavelength. Remarkably, the amplitude of magnetization precession does not go to zero at nodes of these spin waves, which cannot be precisely described by simple analytical formulae. In the steady-state regime, magnetization oscillates with the frequency of the elastic wave, except in the case of longitudinal waves with frequencies well below ν_{res}, where the magnetization precesses with *variable frequency* strongly exceeding the wave frequency. The results obtained for the magnetization dynamics driven by elastic waves are used to calculate the spin current pumped from the dynamically strained ferromagnet into adjacent paramagnetic metal. Numerical calculations demonstrate that the transverse charge current in the paramagnetic layer, which is created by the spin current via inverse spin Hall effect, is high enough to be measured experimentally.

DOI: 10.1103/PhysRevB.94.184401

I. INTRODUCTION

The magnetization dynamics in ferromagnets is usually excited and controlled by magnetic fields or spin-polarized electric currents [1–4]. However, these excitation methods are generally associated with high ohmic energy losses, which make them unsuitable for applications in advanced spintronic devices aimed at low power consumption. Therefore, intensive research efforts are currently focused on the development of alternative excitation techniques, such as exploitation of elastic waves and strain pulses to induce magnetization precession and switching in ferromagnets [5–8]. This "acoustic spintronics" [6], a promising emerging direction in the modern physics of ferromagnets, is based on the magnetoelastic coupling between spins and lattice strains [9], which leads to a variety of interesting physical phenomena. In particular, recent experimental studies revealed dynamic modulations of the magnetization direction by picosecond acoustic pulses [5], spin pumping via injection of sound waves into a ferromagnetic film [6], excitation of a ferromagnetic resonance by surface acoustic waves in a ferromagnetic-ferroelectric hybrid [7], and generation of spin currents at the acoustic resonance [8].

Although the magnetic dynamics driven by elastic waves and strain pulses is inevitably spatially inhomogeneous, this important feature was either ignored in the theoretical studies [7,10,11] or described for special situations in the approximation of small deviations from the equilibrium magnetization direction [12–15]. In this paper, we employed micromagnetic simulations taking into account both magnetoelastic coupling and exchange interaction to describe the inhomogeneous magnetization dynamics excited by standing elastic waves generated in a thin ferromagnetic film. Our simulations not only make it possible to model large-angle magnetization precession but also allow for variations of the dipolar interactions between oscillating spins, which were neglected in the previous papers [12–15]. Computations were carried out for longitudinal and transverse waves in a galfenol film because Fe-Ga alloys have very high magnetoelastic coefficients [16]. The results were used to calculate the time-dependent spin current pumped from the dynamically strained ferromagnet into adjacent paramagnetic metal. It should be noted that standing elastic waves can be created in a thin ferromagnetic film by two counter-propagating surface acoustic waves launched into a piezoelectric substrate using a pair of interdigitated transducers [17]. Furthermore, such waves were generated in plate-like magnetic crystals by femtosecond laser pulses and were found to induce unusual magnetization dynamics [18].

II. MICROMAGNETIC SIMULATIONS OF STRAIN-DRIVEN MAGNETIZATION DYNAMICS

Our approach is based on the numerical integration of the Landau-Lifshitz-Gilbert (LLG) torque equation describing the temporal evolution of the local magnetization $\mathbf{M}(t)$. In the considered case of highly magnetostrictive materials, magnetization dynamics driven by elastic waves can be described by the conventional LLG equation [19], which may be written as $d\mathbf{M}/dt = -\gamma\mathbf{M} \times \mathbf{H}_{\text{eff}} + (\alpha/M_s)\mathbf{M} \times d\mathbf{M}/dt$, where γ is the gyromagnetic ratio, α is the dimensionless Gilbert damping parameter, $M_s = |\mathbf{M}|$ is the saturation magnetization, and $\mathbf{H}_{\text{eff}}$ is the effective magnetic field acting on $\mathbf{M}$. Since at a fixed temperature much lower than the Curie temperature the saturation magnetization may be regarded as a constant quantity, the LLG equation can be reduced to $d\mathbf{m}/dt = -\gamma^*\mathbf{m} \times \mathbf{H}_{\text{eff}} - \alpha\gamma^*\mathbf{m} \times (\mathbf{m} \times \mathbf{H}_{\text{eff}})$, where $\mathbf{m} = \mathbf{M}/M_s$ and $\gamma^* = \gamma/(1+\alpha^2)$.

The effective field $\mathbf{H}_{\text{eff}}$ involved in the LLG equation is the sum of the external magnetic field $\mathbf{H}$, field $\mathbf{H}_{\text{dip}}$ caused by dipolar interactions between spins, and contributions resulting

from the magnetocrystalline anisotropy ($\mathbf{H}_{\rm mca}$), magnetoelastic coupling ($\mathbf{H}_{\rm mel}$), and exchange interaction ($\mathbf{H}_{\rm ex}$). The calculation of $\mathbf{H}_{\rm dip}$ is computationally most time consuming because it requires the summation of magnetic fields created by all spins in the studied ensemble at each spin position. To reduce the simulation time to a reasonable level, we introduce nanoscale computational cells with dimensions much larger than the unit cell size but smaller than the exchange length. The second condition guarantees that the magnetization orientation does not change significantly within an individual cell. Therefore, introduced cells may be modeled by uniformly magnetized rectangular prisms, and the dipolar field $\mathbf{H}_{\rm dip}$ can be calculated as a sum of magnetic fields created by such prisms. Accordingly, $\mathbf{H}_{\rm dip}$ may be written in a general form as

$$\mathbf{H}_{\rm dip}(\mathbf{r}) = \sum_n \mathbf{N}(\mathbf{r}-\mathbf{r}_n)\mathbf{m}(\mathbf{r}_n), \tag{1}$$

where the summation is carried out over all computational cells, $\mathbf{r}_n$ denote the vectors defining the spatial positions of their centers, $\mathbf{m}(\mathbf{r}_n) = \mathbf{m}_n$ is the magnetization direction in the nth cell, and matrix $\mathbf{N}$ is described by analytical relations [20,21]. For the numerical computation of the exchange field $\mathbf{H}_{\rm ex}$, it is convenient to use the relation

$$\mathbf{H}_{\rm ex}(\mathbf{r}_n) = \frac{2A}{M_s}\sum_{p=1}^{6}\frac{\mathbf{m}(\mathbf{r}_p)-\mathbf{m}(\mathbf{r}_n)}{d_p^2}, \tag{2}$$

where A is the exchange stiffness coefficient [22], the summation is carried out over the six nearest neighbors of the nth cell, $d_p = |\mathbf{r}_p - \mathbf{r}_n|$, and the differences between the magnetization orientations in neighboring cells are assumed to be smaller than 30° [23]. The remaining contributions to $\mathbf{H}_{\rm eff} = \mathbf{H} + \mathbf{H}_{\rm mca} + \mathbf{H}_{\rm mel} + \mathbf{H}_{\rm ex} + \mathbf{H}_{\rm dip}$ can be found by differentiating the magnetic energy density F written as a polynomial in terms of the magnetization direction cosines m_i in the Cartesian reference frame (x, y, z) [22]. For ferromagnets with a cubic paramagnetic phase, the relation $\mathbf{H}_{\rm eff} = -\partial F/\partial \mathbf{M}$ gives (no summation over repeated indices $i = x,y,z, j \neq i$ and $k \neq i,j$)

$$H_i^{\rm mca} = -\frac{2}{M_s}\left[K_1\left(m_j^2+m_k^2\right) + K_2 m_j^2 m_k^2\right]m_i, \tag{3}$$

$$H_i^{\rm mel} = -\frac{1}{M_s}[2B_1 u_{ii}m_i + B_2(u_{ij}m_j + u_{ik}m_k)], \tag{4}$$

where K_1 and K_2 are the magnetocrystalline anisotropy constants of fourth and sixth order, B_1 and B_2 are the magnetoelastic coupling constants, and u_{ij} are the lattice strains.

Since the magnetization precession modifies lattice strains, the LLG equation generally should be solved together with the elastodynamic equation of motion [12,13,19]. However, these modifications of lattice strains are very small ($\sim 10^{-4}$–10^{-5}), so we can neglect them when calculating $\mathbf{H}_{\rm mel}$ compared with the strains u_{ij} induced by elastic waves even at $u_{ij} \sim 10^{-3}$. Therefore, the distribution of lattice strains in the film was assumed to be independent of the magnetic pattern. (This approximation does not allow describing the absorption of elastic waves caused by their coupling to the spin system, but this effect is beyond the scope of the present paper.) In

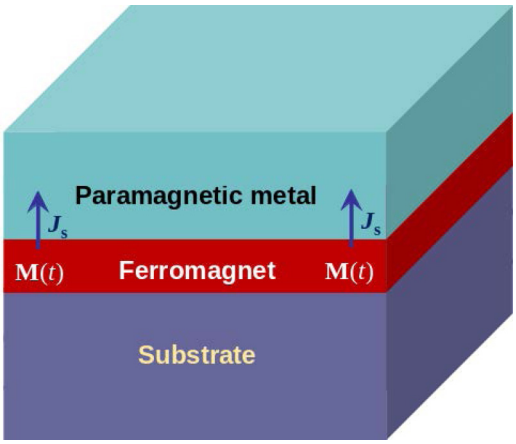

FIG. 1. Schematic representation of a ferromagnetic film grown on a nonmagnetic substrate and covered by a thick layer of paramagnetic metal. Since the magnetization oscillations driven by an elastic wave create a spin current $\mathbf{J}_s$ pumped from the film to the adjacent paramagnetic layer, such a heterostructure may function as an elastically driven spin injector.

our model simulations, two types of standing waves were considered, namely, longitudinal and transverse waves defined by the relations $u_{xx} = u_{\max}\sin(2\pi x/\lambda)\cos(2\pi \nu t)$ and $u_{xz} = u_{zx} = u_{\max}\sin(2\pi x/\lambda)\cos(2\pi \nu t)$, respectively. Strictly speaking, strain waves with such simple structure can exist only in a film sandwiched between two elastic half-spaces with the same elastic properties as the film. However, they also represent a reasonable approximation for elastic waves in a relevant material system having the form of a thin ferromagnetic film grown on a nonmagnetic substrate and covered by a thick layer of paramagnetic metal (see Fig. 1).

The simulations were performed using home-made software which operates with a finite ensemble of N computational cells characterized by their spatial positions $\mathbf{r}_n$ and time-dependent unit vectors $\mathbf{m}_n(t)$ ($n = 1, 2, \ldots, N$). First, the effective fields $\mathbf{H}_{\rm eff}(\mathbf{m}_n)$ acting on vectors $\mathbf{m}_n(t)$ at moment t are calculated with the aid of Eqs. (1)–(4). Using the computed fields and known set of $\mathbf{m}_n(t)$, we integrate the LLG equation numerically and determine the magnetization orientations $\mathbf{m}_n$ at all cells at the moment $t + \delta t$, starting from the equilibrium state of unstrained ferromagnetic film subjected to an elastic wave at $t = 0$. This procedure is repeated until a steady periodic solution for the strain-induced dynamic magnetic pattern is obtained. Since in our case strain distribution has a form of a standing wave, periodic boundary conditions along the x axis may be introduced for a ferromagnetic film parallel to the xy plane, which enables us to consider only cells situated within one wavelength λ (Fig. 2). As a result, the number N of computational cells requiring independent determination of the magnetization orientation $\mathbf{m}_n$ reduces to values ranging from 40 to 1820 depending on the wavelength.

The developed computational scheme employs the LLG equation written in Cartesian coordinates. As the LLG equation is known to be "stiff," a numerical integration is performed using a projective Euler scheme with a fixed integration step $\delta t = 5$ fs, where the condition $|\mathbf{m}| = 1$ is satisfied automatically. To reduce the computation time, dipolar field $\mathbf{H}_{\rm dip}$ is calculated with the aid of fast Fourier transforms and the

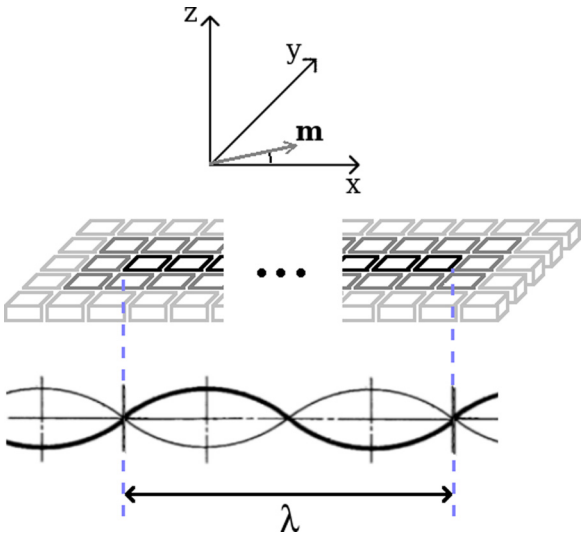

FIG. 2. Schematic of a ferromagnetic film divided into nanoscale computational cells for simulations of the magnetization dynamics induced by standing elastic waves. The axes of the rectangular coordinate system (x, y, z) are parallel to the crystallographic axes of the ferromagnet, the unit vector $\mathbf{m}$ shows the initial orientation of the magnetization, and λ is the wavelength of the standing wave. The ferromagnetic film lies in the xy plane.

convolution theorem. In addition, magnetic fields of uniformly magnetized prisms are replaced by the fields of point magnetic dipoles at distances exceeding the cell sizes by more than a factor of 50. Based on the symmetry of the problem, the orientation of all vectors $\mathbf{m}_n(t)$ in each chain of cells parallel to the in-plane y axis is taken to be the same at each moment t. To test the accuracy of our software, we used it to solve the NIST Standard Problem no. 4 [24] and found good agreement with the reference.

The simulations were performed for 2-nm-thick $Fe_{81}Ga_{19}$ film using the following values of involved material parameters: $M_s = 1321\,\mathrm{emu\,cm^{-3}}$ [25], $\alpha = 0.017$ [26], $A = 1.8 \times 10^{-6}\,\mathrm{erg\,cm^{-1}}$ [27], $K_1 = 1.75 \times 10^5\,\mathrm{erg\,cm^{-3}}$, $K_2 = 0$ [28], $B_1 = -0.9 \times 10^8\,\mathrm{erg\,cm^{-3}}$, and $B_2 = -0.8 \times 10^8\,\mathrm{erg\,cm^{-3}}$ [16]. To stabilize the single-domain initial state in the ferromagnetic film, an external magnetic field with the components $H_x = H_z = 500\,\mathrm{Oe}$ was introduced. Since the exchange length $l_{\mathrm{ex}} = \sqrt{A/(2\pi M_s^2)}$ [29] of $Fe_{81}Ga_{19}$ is about 4 nm, one computational cell is sufficient in the film thickness direction parallel to the z axis. Therefore, we employed cells with dimensions $2 \times 2 \times 2\,\mathrm{nm^3}$ and considered standing elastic waves with wavelengths λ equal to even numbers of the 2-nm cell size only. The frequencies of these waves were determined from the dispersion relation $\nu = c_{l,t}/\lambda$, where the phase velocities $c_l = \sqrt{c_{11}/\rho}$ and $c_t = \sqrt{c_{44}/\rho}$ of longitudinal and transverse waves have been calculated using the elastic stiffnesses $c_{11} = 1.62 \times 10^{12}\,\mathrm{dyne\,cm^{-2}}$, $c_{44} = 1.26 \times 10^{12}\,\mathrm{dyne\,cm^{-2}}$, and density $\rho = 7.8\,\mathrm{g\,cm^{-3}}$ of $Fe_{81}Ga_{19}$ [30]. For both waves, the strain amplitude $u_{\max}$ was set equal to 5×10^{-3}, which is similar to maximal lattice strains arising in picosecond acoustic pulses generated in ferromagnets under femtosecond laser excitation [10].

III. MAGNETIZATION DYNAMICS IN ELASTIC WAVES

The magnetization dynamics caused by the magnetoelastic coupling should depend on the frequency of elastic wave. Therefore, we carried out simulations for standing waves with various wavelengths, which provide a wide frequency

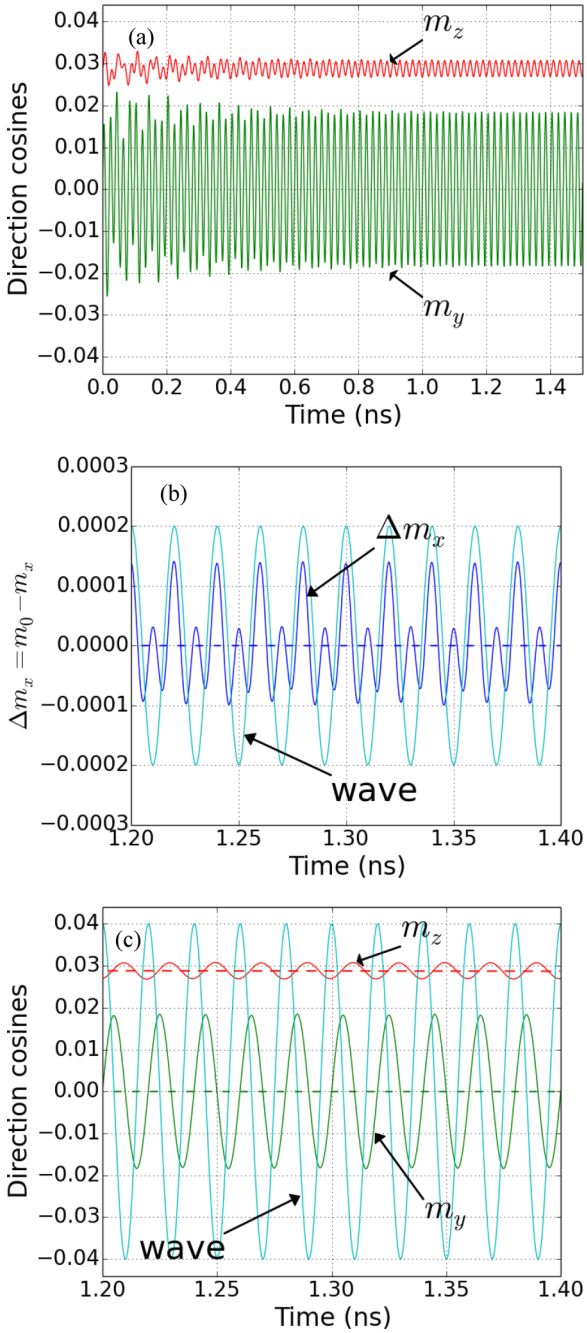

FIG. 3. Magnetization dynamics at the antinode of the transverse standing wave with frequency $\nu \cong 50$ GHz, which is much higher than the resonance frequency $\nu_{\mathrm{res}} \cong 9.89$ GHz of unstrained $Fe_{81}Ga_{19}$ film. Panel (a) shows the temporal evolution of the magnetization direction cosines m_y and m_z in the whole simulation including the transient regime. Panels (b) and (c) present the enlarged view of the regime of steady-state magnetization precession ($m_0 = 0.9995$ is the initial value of the direction cosine m_x). Phase shifts between the periodic variations of the direction cosines m_y and m_z and shear strains in the wave amount to $\pi/2$ and π, respectively.

range spanning frequencies below and above the resonance frequency $\nu_{\rm res}$ of coherent magnetization precession in unstrained $Fe_{81}Ga_{19}$. This resonance frequency was determined by studying the relaxation of the magnetization vector to the equilibrium orientation and found to be about 9.89 GHz at $H_x = H_z = 500$ Oe. It should be emphasized that the external magnetic field was applied along the [101] direction in order to induce nonzero magnetization component m_z, which is needed to make possible the excitation of magnetic dynamics by the longitudinal elastic waves creating the effective field $H_x^{\rm mel} = -2(B_1/M_s)u_{xx}m_x$.

All simulations started at the equilibrium magnetic state of unstrained ferromagnetic film, where the uniform magnetization is directed in the xz plane at an angle of 1.65° with respect to the film surfaces. This initial state transforms into a nonhomogeneous magnetic pattern just upon the introduction of a strain wave at $t = 0$. After a transition period on the order of 1 ns ($\sim 10^5$ simulation steps), the magnetic dynamics acquires the form of a steady-state magnetization precession. The angular deviations from the initial magnetization direction are maximal at the antinodes of standing elastic waves, where the driving force of magnetoelastic origin has the largest value. Remarkably, the magnetization precession does not vanish at the nodes, where the driving force goes to zero, due to cooperative effects caused by exchange and dipolar interactions between spins.

Figure 3 shows the temporal evolution of the magnetization orientation at the antinode ($x = \lambda/4$) of the transverse (shear) standing wave with the frequency $\nu \cong 50$ GHz well above the resonance frequency $\nu_{\rm res}$. It can be seen that the steady magnetization precession, which sets in after a transient regime comprising about 60 oscillations [Fig. 3(a)], occurs with the frequency of elastic wave [Figs. 3(b) and 3(c)]. This feature is due to the fact that the main contribution to the magnetoelastic components $H_x^{\rm mel} = -(B_2/M_s)u_{xz}m_z$ and $H_z^{\rm mel} = -(B_2/M_s)u_{zx}m_x$ of the effective field oscillates with the wave frequency owing to the presence of nonzero mean values of the direction cosines m_z and m_x. The appearance of two maxima of m_x during one period of elastic wave [Fig. 3(b)]

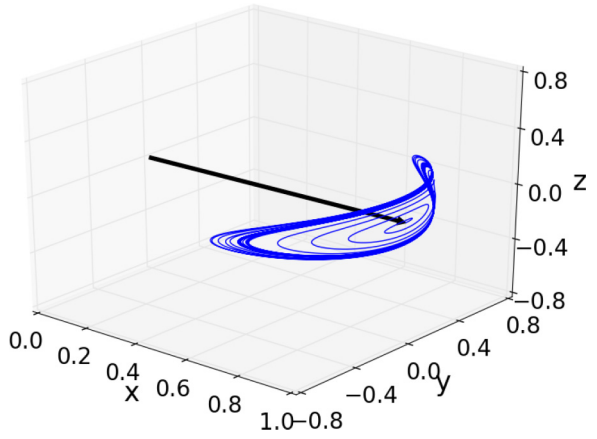

FIG. 4. Typical trajectory of the end of the magnetization vector at the antinodes of transverse standing waves. The three-dimensional plot presents the full trajectory of the unit vector $\mathbf{m} = \mathbf{M}/M_s$ at wave frequency $\nu \cong 9.88$ GHz. The arrow shows the equilibrium magnetization direction.

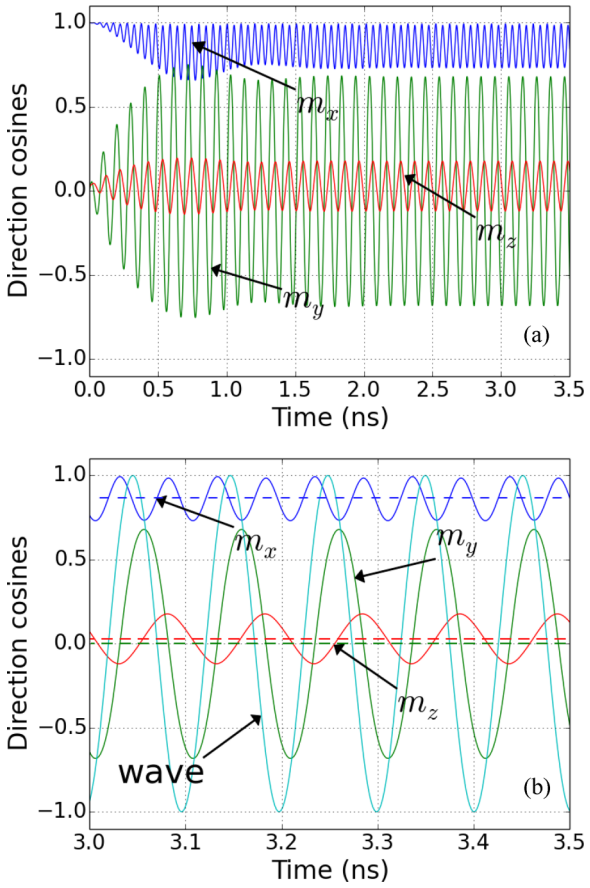

FIG. 5. Temporal evolution of the magnetization orientation at the antinode of the transverse standing wave with frequency $\nu \cong 9.85$ GHz. Panel (a) shows variations of the magnetization direction cosines m_i in the whole simulation including the transient regime, while panel (b) presents the enlarged view of the regime of steady magnetization precession.

results from the specific spatial trajectory of the end of the magnetization vector, which does not have the form of a planar curve (see Fig. 4).

When the frequency of the elastic wave is reduced down to $\nu_{\rm res}$, the magnetization oscillations increase drastically

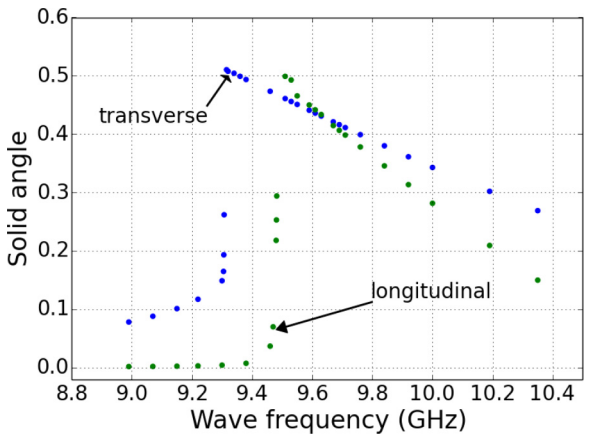

FIG. 6. Frequency dependences of the solid angle of steady-state magnetization precession induced in the $Fe_{81}Ga_{19}$ film at the antinodes of transverse and longitudinal standing waves.

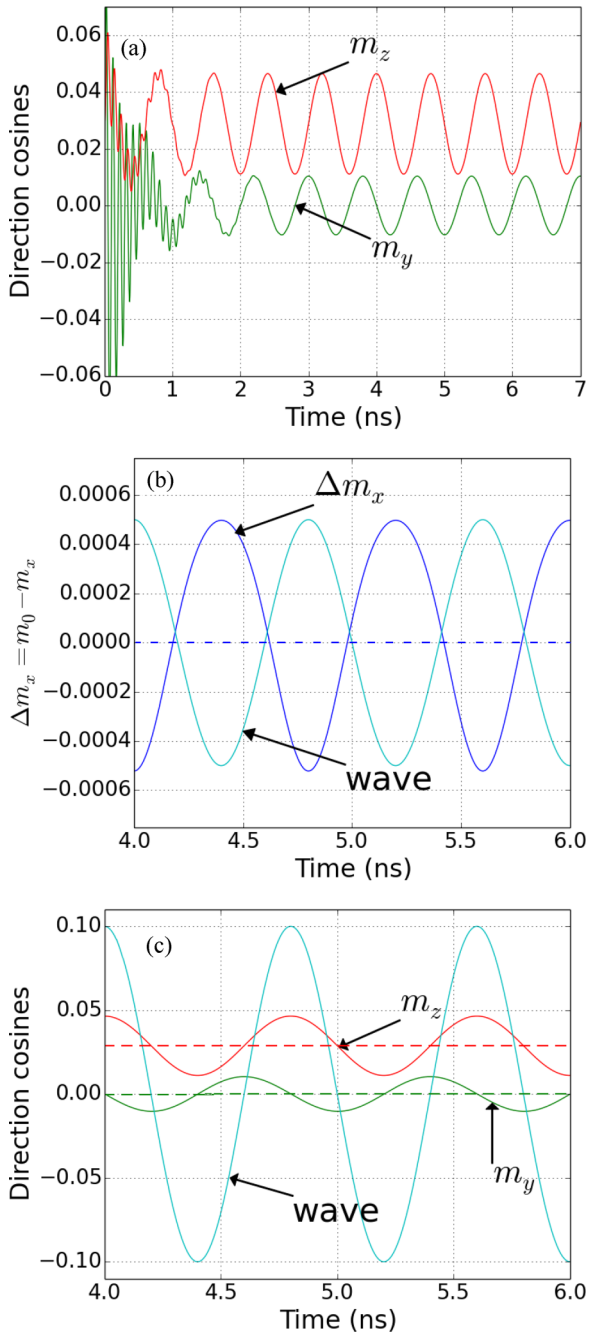

FIG. 7. Magnetization dynamics at the antinode of the transverse standing wave with frequency $\nu \cong 1.25$ GHz. Panel (a) shows the temporal evolution of the magnetization direction cosines m_y and m_z in the whole simulation including the transient regime, while panels (b) and (c) present the enlarged view of the regime of steady magnetization precession.

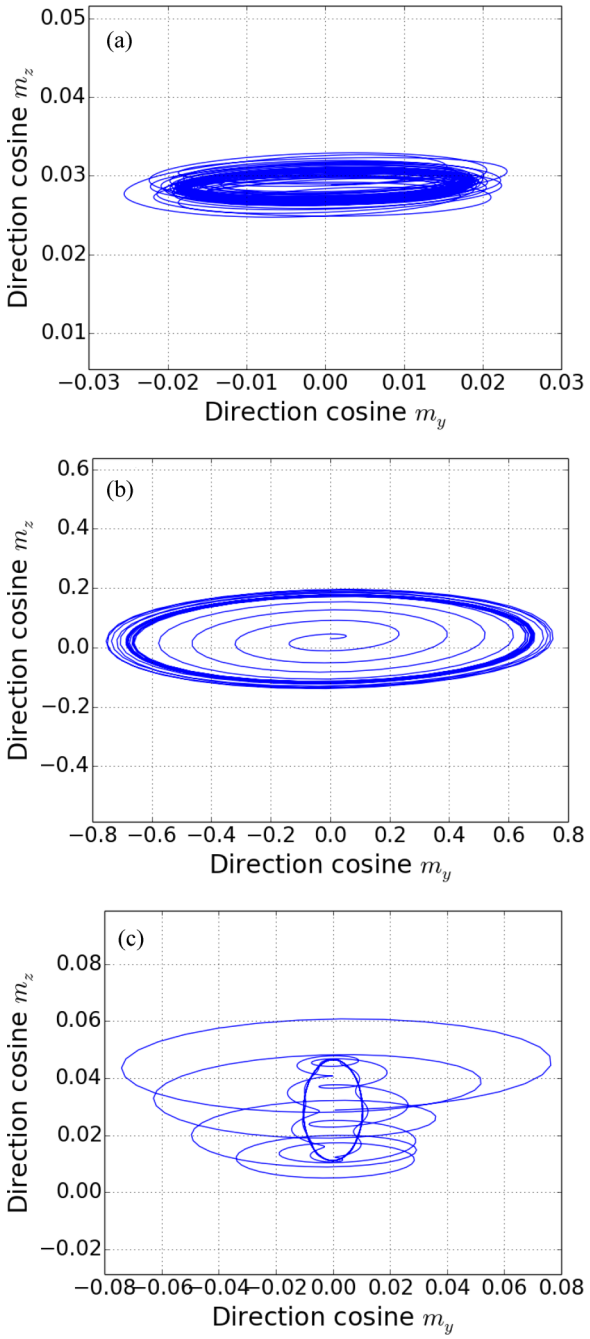

FIG. 8. Magnetization trajectories at the antinodes of transverse standing waves projected on the yz plane orthogonal to their wave vectors. Panels (a), (b), and (c) show the projections of the end of the unit vector $\mathbf{m} = \mathbf{M}/M_s$ calculated at the wave frequencies of 50, 9.85, and 1.25 GHz, respectively.

(Fig. 5). Interestingly, the amplitude of steady magnetization precession reaches a maximum at frequency $\nu_{\max} \cong 9.38$ GHz slightly lower than the resonance frequency of unstrained ferromagnetic film (Fig. 6). At $\nu = \nu_{\max}$, the solid angle of magnetization precession exceeds 0.5, but it decreases rapidly at smaller frequencies, falling down to 0.1 already at $\nu \cong 9.15$ GHz.

Figure 7 illustrates the magnetization dynamics induced by the transverse standing wave with frequency $\nu \cong 1.25$ GHz, which is well below the resonance frequency ν_{res}. A novel feature here is the presence of *double dynamics* in the transient regime [see Fig. 7(a)]. In contrast to the case of $\nu \gg \nu_{\text{res}}$, the magnetization precesses with the frequency $\nu \cong 10$ GHz $\cong \nu_{\text{res}}$, which is much higher than the wave frequency. This fast dynamics is accompanied by slow variations of the precession trajectory following the evolution of elastic wave. In the steady-state regime, the frequency of magnetization precession drops down to the wave frequency [Fig. 7(b)], which is

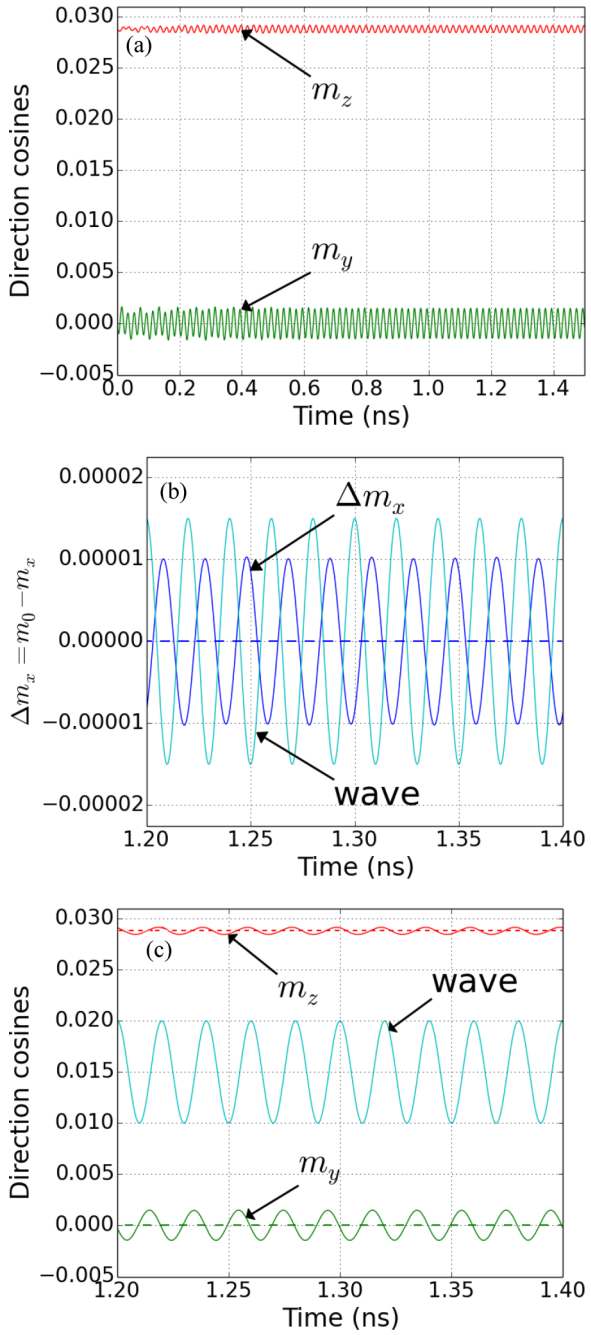

FIG. 9. Magnetization dynamics at the antinode of the longitudinal standing wave with frequency $\nu \cong 50$ GHz excited in the $Fe_{81}Ga_{19}$ film. Panel (a) shows the temporal evolution of the magnetization direction cosines m_y and m_z in the whole simulation including the transient regime, while panels (b) and (c) present the enlarged view of the regime of steady-state magnetization precession.

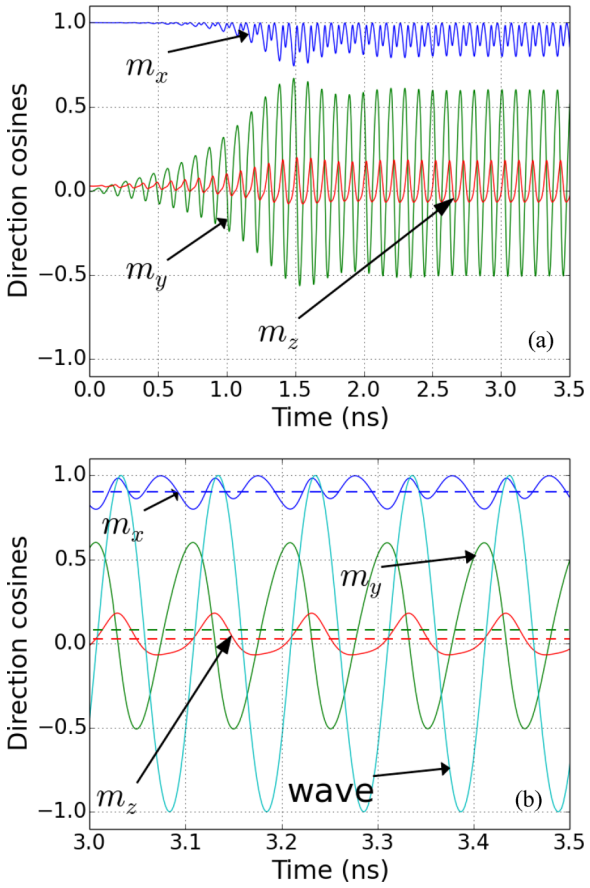

FIG. 10. Temporal evolution of the magnetization orientation at the antinode of the longitudinal standing wave with frequency $\nu \cong 9.89$ GHz. Panel (a) shows variations of the magnetization direction cosines m_i in the whole simulation including the transient regime, while panel (b) presents the enlarged view of the regime of steady magnetization precession.

accompanied by a drastic change in the precession trajectory (see Fig. 8).

The magnetization oscillations excited by longitudinal standing waves with three representative frequencies are shown in Figs. 9–11. At high frequency $\nu \cong 50$ GHz (Fig. 9), the magnetic dynamics is qualitatively similar to that discussed above for the transverse wave with the same frequency. However, angular deviations from the equilibrium magnetization direction are much smaller in the longitudinal wave because this direction only slightly deviates from the x axis in our case. Interestingly, the simulations neglecting variations in the dipolar interactions between spins, which result from spatial inhomogeneity of their oscillations, strongly underestimate the out-of-plane amplitude of magnetization precession, predicting five times smaller changes in the direction cosine m_z. This finding demonstrates that such inhomogeneous variations of the dipolar interactions may strongly influence the elastically driven magnetization dynamics.

At frequencies close to the resonance frequency ν_{res} of unstrained film, the amplitude of magnetization precession strongly increases (Fig. 10). This is accompanied by significant distortions of the time dependences of direction cosines m_i, which remain periodic ($\nu \cong 9.89$ GHz) but cannot be described by simple sine or cosine functions in the steady-state regime. The solid angle of magnetization precession induced by longitudinal waves reaches maximum at the frequency $\nu_{max} \cong 9.61$ GHz, which is slightly higher than the most efficient frequency ν_{max} of transverse waves (see Fig. 6). The most remarkable feature of the resonance curves shown in Fig. 6 is their non-Lorentzian shape. The analysis shows that this strongly asymmetric shape originates from the nonlinear effects, which become important even at moderate

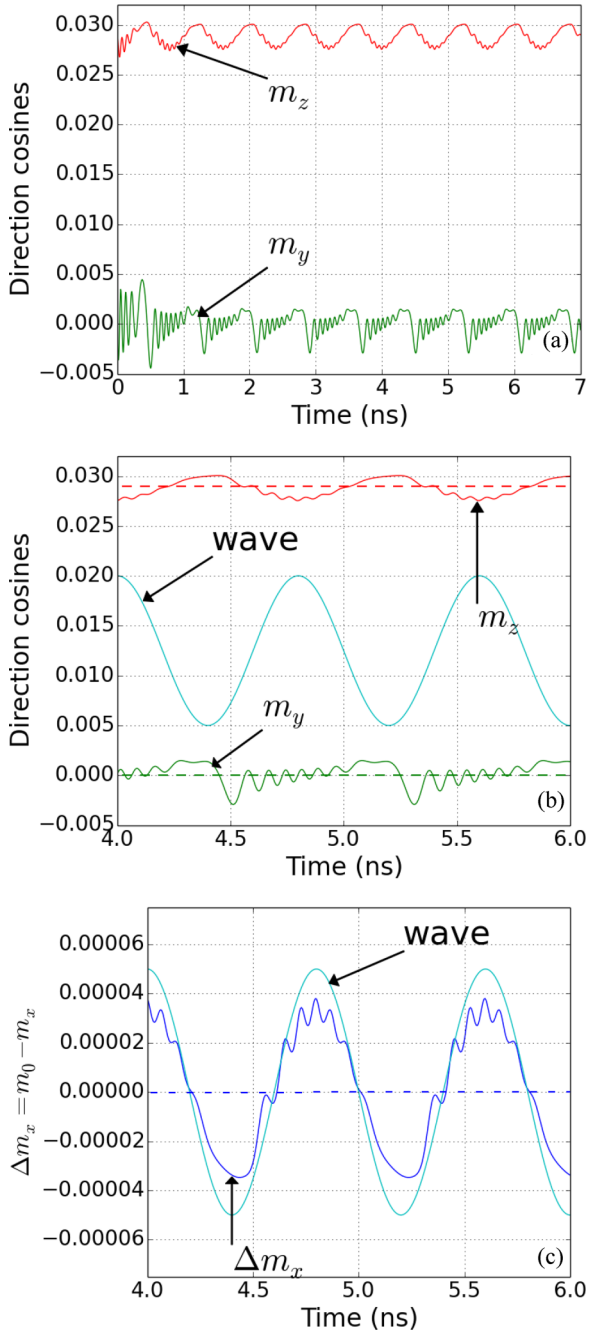

FIG. 11. Magnetization dynamics at the antinode of the longitudinal standing wave with frequency $\nu \cong 1.25$ GHz. Panel (a) shows the temporal evolution of the magnetization direction cosines m_y and m_z in the whole simulation including the transient regime, while panels (b) and (c) present the enlarged view of the regime of steady magnetization precession.

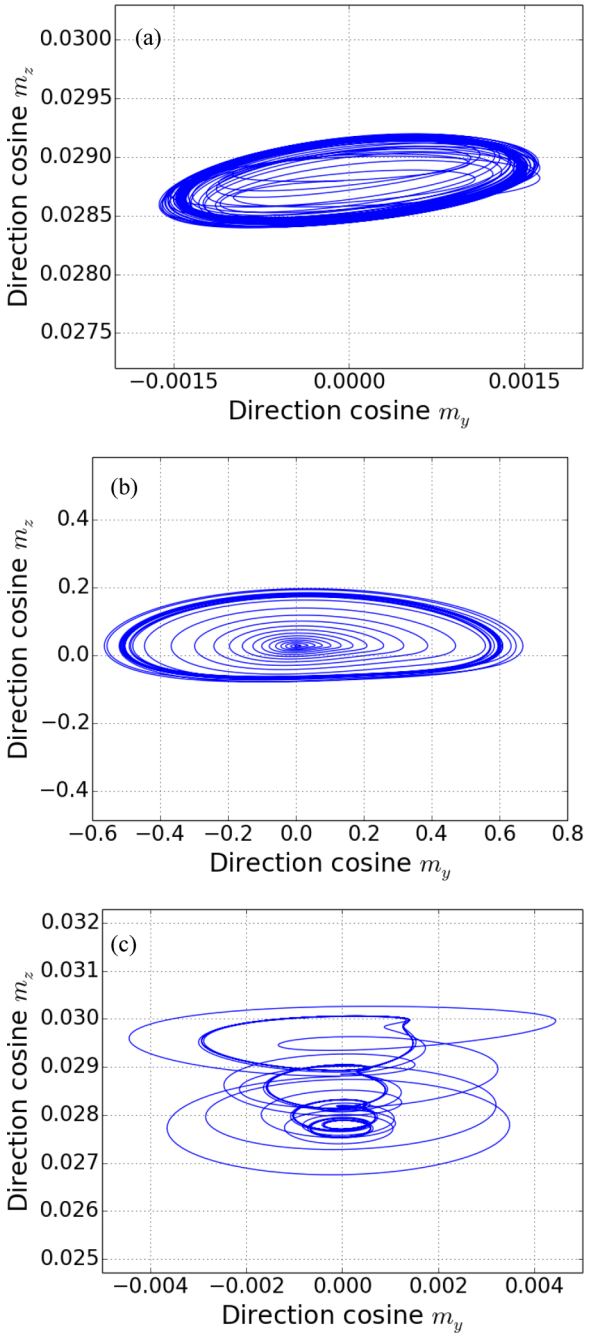

FIG. 12. Magnetization trajectories at the antinodes of longitudinal standing waves projected on the yz plane orthogonal to their wave vectors. Panels (a), (b), and (c) show the projections of the end of the unit vector $\mathbf{m} = \mathbf{M}/M_s$ calculated at the wave frequencies of 50, 9.89, and 1.25 GHz, respectively.

strain amplitudes $u_{\max} \sim 10^{-3}$. Indeed, the resonance curve assumes almost Lorentzian shape in the case of weak elastic excitations creating very small angular deviations of the magnetization from the equilibrium direction even at the wave frequency $\nu = \nu_{\max}$. We also found that the simulations based on the linearized LLG equation, where the right-hand side is approximated by a linear function of the direction cosine variations δm_i near their equilibrium values, give unphysical results for the elastic waves with $u_{\max} = 5 \times 10^{-3}$ and frequencies close to ν_{res}, erroneously predicting the strain-driven magnetization reorientation against the applied magnetic field ($m_x < 0$ at $H_x > 0$).

When the frequency of the longitudinal wave is reduced below ν_{res}, the magnetic dynamics changes dramatically (Fig. 11). Most importantly, the magnetization precesses with a *variable frequency* strongly exceeding the wave frequency. This feature may be attributed to the dependence of the resonance frequency ν_{res} of coherent precession on lattice strains [31]. Indeed, analytical calculation shows that the

change of u_{xx} from –0.005 to +0.005 gives $\nu_{\rm res}$ ranging from 3.44 to 14.45 GHz, which agrees with the frequency range 4.3−15 GHz obtained from the micromagnetic simulations. These frequency variations are accompanied by periodic changes of the precession trajectory following the evolution of the elastic wave. In contrast to the case of transverse waves, this double dynamics does not disappear in the steady-state regime (see Fig. 11). The magnetization trajectories at three representative frequencies of longitudinal waves are compared in Fig. 12.

In conclusion of this section, we consider spatial distributions of the magnetization oscillations in standing elastic waves. Figures S1 and S2 in the Supplemental Material [32] demonstrate that such elastic excitations generate *standing spin waves* with the same wavelength. Remarkably, the amplitude of magnetization precession does not go to zero at the nodes of these spin waves. Of course, the precession amplitude is always much larger at antinodes than at nodes, but the ratio of the amplitude at an antinode to that at a node decreases strongly when the frequency of the elastic wave increases from $\nu \ll \nu_{\rm res}$ to $\nu \gg \nu_{\rm res}$. The movies of Figs. S1 and S2 [32] further show that the elastically generated standing spin waves may have very complex structure, especially when excited by a longitudinal elastic wave. In all cases, these spin waves cannot be precisely described by simple relations of the form $m_i(x,t) = m_i^0 + \delta m_i \sin(2\pi x/\lambda)\cos(2\pi\nu t)$. To gain additional information on their structure, we performed the Fourier analysis of the spatial distributions of m_i formed at the moment when the strain at the antinodes of the elastic wave reaches its maximum value. The calculations showed that, in the case of spin wave induced by the transverse elastic wave with the frequency $\nu \ll \nu_{\rm res}$, a term proportional to $\sin(2\pi x/\lambda)$ is sufficient to describe the direction cosines $m_y(x)$ and $m_z(x)$ with good accuracy. This term also provides the main contribution to $m_y(x)$ and $m_z(x)$ in spin waves generated by transverse and longitudinal elastic waves with frequencies $\nu \geqslant \nu_{\rm res}$, but here a significant additional contribution (up to 30% of the leading term) is caused by a term proportional to $\sin(6\pi x/\lambda)$. At the same time, in the spin wave excited by the longitudinal elastic wave with $\nu \ll \nu_{\rm res}$, the distribution of $m_y(x)$ may be approximated by the sum of terms proportional to $\sin(4\pi x/\lambda)$ and $\sin(20\pi x/\lambda)$, while an approximate description of $m_z(x)$ requires terms proportional to $\sin(2\pi x/\lambda)$ and $\sin(8\pi x/\lambda)$.

Consider, finally, the possible influence of the spin-wave dispersion relation on the elastically driven magnetization dynamics. The analysis shows that, in our case, the dependence of the spin-wave frequency $\nu_{\rm sw}$ on the wavenumber $k_{\rm sw}$ may be approximated by the formula

$$\nu_{\rm sw} \approx \frac{\gamma}{2\pi}\sqrt{\left[H_x + H_z + \frac{2K_1}{M_s} + \frac{2A}{M_s}k_{\rm sw}^2 + 4\pi M_s\left(1 - \frac{1}{2}k_{\rm sw}d\right)\right]\left(H_x + \frac{2K_1}{M_s} + \frac{2A}{M_s}k_{\rm sw}^2\right)}, \tag{5}$$

which is a modified version of the dispersion relation [33] taking into account both the exchange coupling and dipolar interactions between oscillating spins (d is the film thickness). Since our simulations showed that the wavelength of the spin wave always coincides with that of the driving elastic wave, the wavenumber $k_{\rm sw}$ can be calculated as $k_{\rm sw} = 2\pi\nu/c_{t,l}$. Using this relation together with Eq. (5), we evaluated the spin-wave frequencies corresponding to different frequencies ν of the standing elastic waves. It was found that the difference between $\nu_{\rm sw}$ and the resonance frequency $\nu_{\rm res}$ of coherent precession remains small (∼0.5 GHz), even at $\nu \sim \nu_{\rm res}$. Therefore, the influence of the dispersion relation on the elastically driven magnetization dynamics is hardly detectable at $\nu \leqslant \nu_{\rm res}$. However, the difference $\nu_{\rm sw} - \nu_{\rm res}$ becomes rather large (7−8 GHz) at the high frequency $\nu =$ 50 GHz, which should manifest itself in the transient regime of magnetization dynamics at such elastic-wave frequency. To check this expectation, we performed the Fourier analysis of the transient regime in the time domain and found that the Fourier spectrum contains a weak component oscillating with a frequency well below 50 GHz, which shows up in slight beatings of the precession amplitude. The frequency of this component is about 18 GHz in the case of transverse elastic wave and about 17 GHz for the longitudinal one. These values are in good agreement with the spin-wave frequencies given by Eq. (5), which confirms the expected influence of the dispersion relation. It should be noted that the dipolar interactions considerably reduce the difference $\nu_{\rm sw} - \nu_{\rm res}$ via the term $-2\pi M_s k_{\rm sw} d$, whereas the magnetoelastic coupling is expected to have a negligible effect on the spin-wave frequencies in our case according to the numerical estimates based on the dispersion relation reported in Ref. [15].

IV. SPIN PUMPING DRIVEN BY ELASTIC WAVES

When a ferromagnet is in contact with a paramagnetic metal, magnetization precession in the former leads to a spin pumping into the latter [34]. The spin current density $\mathbf{I}_s$ at the interface can be calculated from the relation [34–36]

$$\begin{aligned}\mathbf{I}_s &= i_s\mathbf{s} \\ &= \frac{\hbar}{4\pi}\left(\mathrm{Re}[g_{\uparrow\downarrow}^r - g_{\uparrow\downarrow}^t]\mathbf{m}\times\frac{d\mathbf{m}}{dt} + \mathrm{Im}[g_{\uparrow\downarrow}^r - g_{\uparrow\downarrow}^t]\frac{d\mathbf{m}}{dt}\right),\end{aligned} \tag{6}$$

where $\mathbf{s}$ is the unit vector of spin-current polarization, and $g_{\uparrow\downarrow}^r$, $g_{\uparrow\downarrow}^t$ are the complex reflection and transmission spin mixing conductances per unit contact area [37,38]. According to Eq. (6), the magnetization precession induced by elastic waves should create a spin current comprising dc and ac components. The results of our micromagnetic simulations enable us to calculate both dc and ac spin currents generated by standing elastic waves. Since the first-principles studies of spin mixing conductances [38] show that $g_{\uparrow\downarrow}^t$ and the imaginary part of $g_{\uparrow\downarrow}^r$ should be negligible for the 2-nm-thick ferromagnetic film considered in this paper, in our calculations we used the

approximate relation

$$\mathbf{I}_s \cong \frac{\hbar}{4\pi}\mathrm{Re}[g^r_{\uparrow\downarrow}]\mathbf{m} \times \frac{d\mathbf{m}}{dt}. \quad (7)$$

Figure 13(a) shows the time dependence of the spin current created at the antinode of the transverse standing wave with a frequency close to ν_{res}. It can be seen that, in the steady-state regime, all three components s_i of the spin-current polarization $\mathbf{s}$ oscillate with the wave frequency. Interestingly, the oscillations of the spin-current component $I^s_z(t)$ have much larger amplitudes than the oscillations of $I^s_y(t)$ and $I^s_x(t)$. However, only the projection of the spin current on the x axis has a significant mean value. To determine mean values $\bar{I}^s_i$ of all three spin-current components, we averaged $I^s_i(t)$ during the time period comprising several oscillations [see Fig. 13(b)]. It was found that in the steady-state regime $\bar{I}^s_x \approx (2\hbar/\pi)\mathrm{Re}[g^r_{\uparrow\downarrow}]\,\mathrm{ns}^{-1}$, $\bar{I}^s_z \approx (0.05\hbar/\pi)\mathrm{Re}[g^r_{\uparrow\downarrow}]\,\mathrm{ns}^{-1}$, while $\bar{I}^s_y$ is negligible. These results can be explained by the fact that, according to Eq. (7), the dc component of the spin current should be parallel to the axis of magnetization precession. In the considered case, the latter is close to the equilibrium magnetization in the unstrained film, which is almost parallel to the x axis, having an additional small projection on the z axis only.

Since the quantity relevant to experimental measurements is the spin current produced by a macroscopic section of the film, we calculated the average current density $\langle I^s_i\rangle$ pumped from the film region corresponding to one wavelength λ. Figure 13(c) demonstrates that this averaging strongly reduces the y and z components of the spin current and doubles the frequency of spin-current oscillations. The frequency doubling happens because the spin-current components averaged over the first and second halves of the standing elastic wave oscillate in the opposite phase and have nonsinusoidal time dependences. The filtering of high-frequency oscillations [see Fig. 13(d)] further shows that the x component retains a significant mean value $\langle \bar{I}^s_x\rangle \approx 0.8(\hbar/\pi)\mathrm{Re}[g^r_{\uparrow\downarrow}]\,\mathrm{ns}^{-1}$, which is only about two times smaller than $\bar{I}^s_x$ at the antinode of the transverse standing wave. This feature is due to magnetization precession happening in a counterclockwise direction everywhere despite opposite signs of the driving field $\mathbf{H}_{\mathrm{mel}}$ in two halves of the standing wave. It should be noted that, according to our preliminary simulations of the elastically driven magnetization dynamics at finite temperatures, which were realized by adding a fluctuating thermal field [23] to the effective field $\mathbf{H}_{\mathrm{eff}}$ involved in the LLG equation, the mean spin-current density $\langle \bar{I}^s_x\rangle$ is expected to have similar magnitude at room temperature as well.

The results obtained for spin currents driven by the longitudinal elastic wave with the frequency close to ν_{res} are shown in Fig. 14. It can be seen that they are essentially similar to the results discussed above, but with two interesting distinctions. First, the mean values $\bar{I}^s_y$ and $\langle \bar{I}^s_y\rangle$ of the y component are not negligible in the steady-state regime, being close to those of the z component of the spin current [see Figs. 15(b) and 15(d)]. This feature is caused by the fact that the axis of magnetization precession driven by the longitudinal wave has a nonzero projection on the y axis. Second, in contrast to the case of the transverse wave, the averaging of the pumped spin current over the wavelength λ leaves

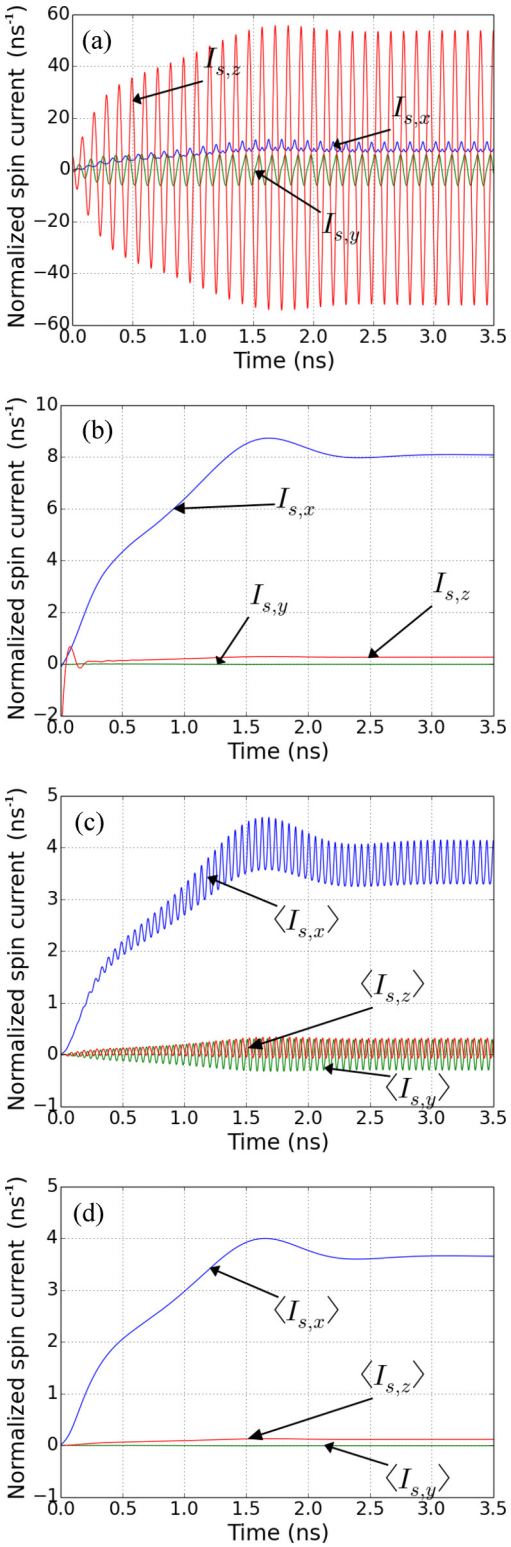

FIG. 13. Time dependence of the spin current generated by the $Fe_{81}Ga_{19}$ film subjected to the transverse elastic wave with frequency 9.38 GHz. The components I^s_i of the spin-current density are normalized by the quantity $(\hbar/4\pi)\mathrm{Re}[g^r_{\uparrow\downarrow}]$. Panels (a) and (b) show I^s_i at the antinode of the standing wave, while panels (c) and (d) present the current density averaged over one wavelength of this elastic wave. The direct results of calculations are given in panels (a) and (c), whereas panels (b) and (d) show mean current densities obtained after filtering out high-frequency oscillations.

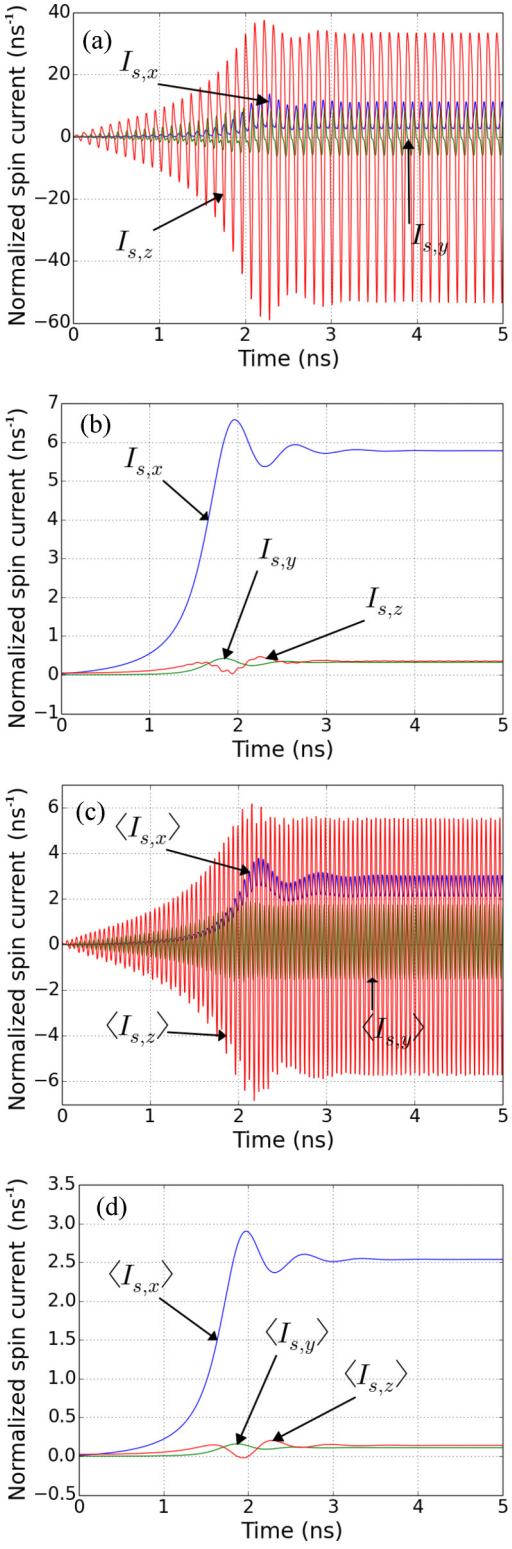

FIG. 14. Time dependence of the spin current generated by the $Fe_{81}Ga_{19}$ film subjected to the longitudinal elastic wave with frequency 9.61 GHz. The components I_i^s of the spin-current density are normalized by the quantity $(\hbar/4\pi)\mathrm{Re}[g^r_{\uparrow\downarrow}]$. Panels (a) and (b) show I_i^s at the antinode of the standing wave, while panels (c) and (d) present the current density averaged over one wavelength of this elastic wave. The direct results of calculations are given in panels (a) and (c), whereas panels (b) and (d) show mean current densities obtained after filtering out high-frequency oscillations.

the amplitude of the $\langle I_z^s\rangle$ oscillations larger than the $\langle I_x^s\rangle$ component [compare Figs. 13(c) and 14(c)]. Nevertheless, the mean value $\langle \bar{I}_x^s\rangle \approx 0.6(\hbar/\pi)\mathrm{Re}[g^r_{\uparrow\downarrow}]\,\mathrm{ns}^{-1}$ of the averaged x component remains much larger than the mean value $\langle \bar{I}_z^s\rangle \approx 0.025(\hbar/\pi)\mathrm{Re}[g^r_{\uparrow\downarrow}]\,\mathrm{ns}^{-1}$ of the z component.

Using the theoretical result $(e^2/h)\mathrm{Re}[g^r_{\uparrow\downarrow}] \approx 4.66 \times 10^{14}\,\Omega^{-1}\mathrm{m}^{-2}$ obtained for the reflection spin mixing conductance of the Fe/Au interface by first-principles calculations [38], we estimated numerical values of the spin currents pumped from the dynamically strained $Fe_{81}Ga_{19}$ film into adjacent Au layer. In particular, calculations give $\langle \bar{I}_x^s\rangle/\hbar \approx 3.4 \times 10^{27}\,\mathrm{s}^{-1}\mathrm{m}^{-2}$ for the mean current density generated by the transverse elastic wave with the frequency $\nu = 9.38$ GHz and $\langle \bar{I}_x^s\rangle/\hbar \approx 2.4 \times 10^{27}\,\mathrm{s}^{-1}\mathrm{m}^{-2}$ for the longitudinal wave with $\nu = 9.61$ GHz. These estimates render it possible to evaluate the dc charge current created in the Au layer by the pumped spin current due to the inverse spin Hall effect. The density $\mathbf{I}_c$ of the charge current is given by the relation $\mathbf{I}_c = \alpha_{\mathrm{SH}}(2e/\hbar)(\mathbf{e}_s \times \mathbf{I}_s)$, where α_{SH} is the spin Hall angle, e denotes the elementary positive charge, and $\mathbf{e}_s$ is the unit vector in the spin current direction [36]. Hence, the charge current is orthogonal to the spin current and almost parallel to the y axis in our case. Taking $\alpha_{\mathrm{SH}} \approx 0.0035$ for Au [39], we find the current density $\langle \bar{I}_y^c\rangle_{z=0}$ generated at the interface by the transverse and longitudinal waves to be about 3.9×10^6 and 2.7×10^6 A m^{-2}, respectively. Since the injected spin current decays inside normal metal due to spin relaxation and diffusion, the density of charge current falls with distance from the interface [40]. The total charge current in the normal metal layer of width w_N and thickness t_N can be found from the relation

$$\langle \bar{J}_y^c\rangle = \langle \bar{I}_y^c\rangle_{z=0}\xi_{\mathrm{sd}} w_N \frac{\cosh[t_N/\xi_{\mathrm{sd}}] - 1}{\sinh[t_N/\xi_{\mathrm{sd}}]}, \tag{8}$$

where ξ_{sd} is the spin diffusion length. Taking $\xi_{\mathrm{sd}} = 35$ nm for Au [40] and assuming $w_N = 10\ \mu$m, we obtain the total charge current generated in the Au layer with $t_N > 5\xi_{\mathrm{sd}}$ by the considered standing elastic waves to be about 1 μA, which can be readily measured experimentally.

V. CONCLUDING REMARKS

In this paper, we carried out micromagnetic simulations of the inhomogeneous magnetization dynamics induced in a ferromagnetic material by elastic waves. In contrast to the preceding analytical treatments of the problem [12–15], our calculations do not involve the assumption of small deviations from the equilibrium magnetization direction. By solving the LLG equation numerically, we simulated the magnetic dynamics induced by transverse and longitudinal standing waves generated in the 2-nm-thick $Fe_{81}Ga_{19}$ film sandwiched between two elastic half-spaces. Both the transient and steady-state regimes of magnetization oscillations are described in detail.

The simulations showed that elastic waves induce strongly inhomogeneous magnetization precession, which acquires maximal amplitude at the antinodes of standing waves (near the antinodes in the case of transverse waves with frequencies $\nu \gg \nu_{\mathrm{res}}$). This amplitude increases drastically near the resonance frequency ν_{res} of the unstrained ferromagnetic film (Fig. 6),

reaching a maximum at $\nu = \nu_{max} < \nu_{res}$. Surprisingly, the resonance curve has a strongly asymmetric, non-Lorentzian shape, which is due to the nonlinear effects. Therefore, the solid angle of steady-state magnetization precession decreases rather slowly with increasing wave frequency at $\nu > \nu_{max}$. This feature provides effective elastic excitation of the magnetization dynamics in a finite range of wave frequencies $\nu_{max} \leqslant \nu \leqslant \nu_{max} + \delta\nu$ with a considerable width $\delta\nu \sim 1$ GHz.

In the steady-state regime, the frequency of magnetization oscillations equals that of the driving elastic wave, except in the case of longitudinal waves with frequencies well below ν_{res}, where the magnetization precesses with a variable frequency strongly exceeding the wave frequency [Fig. 11(c)]. The spatial distributions of magnetization oscillations in the considered elastic waves have the form of standing spin waves with the same wavelength λ (see Supplemental Material [32]). Importantly, the simulations demonstrate that the structure of an elastically generated spin wave may be very different from that of the driving elastic wave. Our qualitative predictions should be valid for all ferromagnetic materials with strong magnetoelastic coupling, such as FeCo alloys and nickel.

Using the results obtained for the magnetic dynamics induced by elastic waves, we also calculated the spin currents that can be pumped from the dynamically strained $Fe_{81}Ga_{19}$ film into the adjacent layer of paramagnetic metal. It was found that both transverse and longitudinal standing waves with a frequency close to ν_{res} create spin currents comprising significant dc and ac components. Interestingly, the spin polarization of the dc component is not exactly parallel to the equilibrium magnetization direction in the steady-state regime. The calculations of the transverse charge current, which is created by the spin current via the inverse spin Hall effect, showed that the charge current has high density at the interface and can be easily measured experimentally.

ACKNOWLEDGMENT

This research was supported by the Government of the Russian Federation through the program P220 (Project No. 14.B25.31.0025; leading scientist A. K. Tagantsev).

[1] M. Farle, Rep. Prog. Phys. **61**, 755 (1998).
[2] J. C. Slonczewski and J. Z. Sun, J. Magn. Magn. Mater. **310**, 169 (2007).
[3] A. Brataas, A. D. Kent, and H. Ohno, Nature Materials **11**, 372 (2012).
[4] W. H. Rippard, M. R. Pufall, S. Kaka, S. E. Russek, and T. J. Silva, Phys. Rev. Lett. **92**, 027201 (2004).
[5] A. V. Scherbakov, A. S. Salasyuk, A. V. Akimov, X. Liu, M. Bombeck, C. Brüggemann, D. R. Yakovlev, V. F. Sapega, J. K. Furdyna, and M. Bayer, Phys. Rev. Lett. **105**, 117204 (2010).
[6] K. Uchida, H. Adachi, T. An, T. Ota, M. Toda, B. Hillebrands, S. Maekawa, and E. Saitoh, Nature Materials **10**, 737 (2011).
[7] M. Weiler, L. Dreher, C. Heeg, H. Huebl, R. Gross, M. S. Brandt, and S. T. B. Goennenwein, Phys. Rev. Lett. **106**, 117601 (2011).
[8] M. Weiler, H. Huebl, F. S. Goerg, F. D. Czeschka, R. Gross, and S. T. B. Goennenwein, Phys. Rev. Lett. **108**, 176601 (2012).
[9] N. Akulov, Z. Phys. **52**, 389 (1928).
[10] T. L. Linnik, A. V. Scherbakov, D. R. Yakovlev, X. Liu, J. K. Furdyna, and M. Bayer, Phys. Rev. B **84**, 214432 (2011).
[11] L. Thevenard, J.-Y. Duquesne, E. Peronne, H. J. von Bardeleben, H. Jaffres, S. Ruttala, J.-M. George, A. Lemaître, and C. Gourdon, Phys. Rev. B **87**, 144402 (2013).
[12] A. I. Akhiezer, V. G. Bar'iakhtar, and S. V. Peletminski, J. Exptl. Theoret. Phys. (U.S.S.R.) **35**, 228 (1958) [Sov. Phys. JETP **35**, 157 (1959)].
[13] C. Kittel, Phys. Rev. **110**, 836 (1958).
[14] L. Dreher, M. Weiler, M. Pernpeintner, H. Huebl, R. Gross, M. S. Brandt, and S. T. B. Goennenwein, Phys. Rev. B **86**, 134415 (2012).
[15] A. Kamra, H. Keshtgar, P. Yan, and G. E. W. Bauer, Phys. Rev. B **91**, 104409 (2015).
[16] J. B. Restorff, M. Wun-Fogle, K. B. Hathaway, A. E. Clark, T. A. Lograsso, and G. Petculescu, J. Appl. Phys. **111**, 023905 (2012).
[17] J. Dean, M. T. Bryan, J. D. Cooper, A. Virbule, J. E. Cunningham, and T. J. Hayward, Appl. Phys. Lett. **107**, 142405 (2015).
[18] D. Afanasiev, I. Razdolski, K. M. Skibinsky, D. Bolotin, S. V. Yagupov, M. B. Strugatsky, A. Kirilyuk, Th. Rasing, and A. V. Kimel, Phys, Rev. Lett. **112**, 147403 (2014).
[19] Y. V. Gulyaev, I. E Dikshtein, and V. G Shavrov, Phys.-Usp. **40**, 701 (1997).
[20] A. J. Newell, W. Williams, and D. J. Dunlop, J. Geophys. Res.: Solid Earth **98**, 9551 (1993).
[21] M. J. Donahue, *6th International Symposium on Hysteresis Modeling and Micromagnetics HMM-2007* (Naples, Italy, 2007), http://math.nist.gov/~MDonahue/talks/hmm2007-MBO-03-accurate_demag.pdf.
[22] C. Kittel, Rev. Mod. Phys. **21**, 541 (1949).
[23] A. Vansteenkiste, J. Leliaert, M. Dvornik, M. Helsen, F. Garcia-Sanchez, and B. Van Waeyenberge, AIP Advances **4**, 107133 (2014).
[24] See http://www.ctcms.nist.gov/~rdm/std4/spec4.html.
[25] J. Atulasimha and A. B Flatau, Smart Mater. Struct. **20**, 043001 (2011).
[26] J. V. Jager, A. V. Scherbakov, T. L. Linnik, D. R. Yakovlev, M. Wang, P. Wadley, V. Holy, S. A. Cavill, A. V. Akimov, A. W. Rushforth, and M. Bayer, Appl. Phys. Lett. **103**, 032409 (2013).
[27] K. S. Narayan, Master's thesis, University of Minnesota, 2010, http://conservancy.umn.edu/bitstream/handle/11299/93191/Krishnan_Shankar_May2010.pdf.
[28] G. Petculescu, K. B. Hathaway, T. A. Lograsso, M. Wun-Fogle, and A. E. Clark, J. Appl. Phys. **97**, 10M315 (2005).
[29] C. A. F. Vaz, J. A. C. Bland, and G. Lauhoff, Rep. Prog. Phys. **71**, 056501 (2008).
[30] R. R. Basantkumar, B. J. H. Stadler, R. William, and E. Summers, IEEE Trans. Magn. **42**, 3102 (2006).
[31] N. A. Pertsev, H. Kohlstedt, and R. Knöchel, Phys. Rev. B **84**, 014423 (2011).

[32] See Supplemental Material at http://link.aps.org/supplemental/10.1103/PhysRevB.94.184401 for movies of spin waves excited by transverse and longitudinal standing elastic waves.
[33] R. L. Stamps and B. Hillebrands, Phys. Rev. B **44**, 12417 (1991).
[34] Y. Tserkovnyak, A. Brataas, G. E.W. Bauer, and B. Halperin, Rev. Mod. Phys. **77**, 1375 (2005).
[35] Y. Tserkovnyak, A. Brataas, and G. E. W. Bauer, Phys. Rev. B **66**, 224403 (2002).
[36] H. J. Jiao and G. E. W. Bauer, Phys. Rev. Lett. **110**, 217602 (2013).
[37] A. Brataas, Yu. V. Nazarov, and G. E. W. Bauer, Phys. Rev. Lett. **84**, 2481 (2000).
[38] M. Zwierzycki, Y. Tserkovnyak, P. J. Kelly, A. Brataas, and G. E. W. Bauer, Phys. Rev. B **71**, 064420 (2005).
[39] O. Mosendz, V. Vlaminck, J. E. Pearson, F. Y. Fradin, G. E. W. Bauer, S. D. Bader, and A. Hoffmann, Phys. Rev. B **82**, 214403 (2010).
[40] O. Mosendz, J. E. Pearson, F. Y. Fradin, G. E. W. Bauer, S. D. Bader, and A. Hoffmann, Phys. Rev. Lett. **104**, 046601 (2010).